PLOS Climate

RESEARCH ARTICLE

Quantification of natural CO_2 emissions from mofettes using a low-cost sensor network at the Starzach site in South-West Germany

Yann Georg Büchau*, Jens Bange

Department of Geoscience, University of Tübingen, Tübingen, Baden-Württemberg, Germany

* yann-georg.buechau@uni-tuebingen.de

Citation: Büchau YG, Bange J (2025) Quantification of natural CO_2 emissions from mofettes using a low-cost sensor network at the Starzach site in South-West Germany. PLOS Clim 4(11): e0000741. https://doi.org/10.1371/journal.pclm.0000741

Editor: Zhihua Zhang, Shandong University, CHINA

Received: September 4, 2025

Accepted: October 17, 2025

Published: November 25, 2025

Data availability statement: Analysed data is available at https://doi.org/10.5281/zenodo.17055782.

Funding: This work was supported by the DFG under grant number BA 1988/19-1.

Abstract

We present a top-down method to derive CO_2 emissions from mofettes, using only point measurement time series at irregular locations. Notably, no wind vector information is needed, as gas transport is derived from cross-correlations between sensor stations and subsequently integrated using Gauss' divergence theorem. The method is applied to an existing low-cost sensor network at the Starzach site near the Black Forest in Germany, for which no comprehensive estimate of the total emissions exists yet. For validation, we use previous bottom-up measurements of individual mofette degassing and a Gaussian puff approach. Over a period of one and a half months around August 2022, we determine an average CO_2 emission rate of $3266\,\mathrm{kg\,d^{-1}} \pm 42\%$ over a $400\,\mathrm{m}^2$ area. This result is larger than expected and suggests that diffuse degassing plays a more important role at site than previously assumed. The method could also be applied for real-time monitoring of leaky CCS sites, for which the Starzach site is a natural analog.

Introduction

The greenhouse gases (GHGs) CO_2, methane (CH_4) and nitrous oxide (N_2O) are major drivers of global warming [1,2], with CO_2 having the strongest effect due to its increasingly high concentration in the Earth's atmosphere. Location and quantification of GHG emission sources is thus a vital step in identifying hotspots and verification of reduction methods. Both are tasks the countries under the Paris Agreement [3] have committed to, by keeping up-to-date emission inventories. In Germany for example, the Integrated Greenhouse Gas Monitoring System for Germany (ITMS) is a project working towards these tasks [4–6].

There is no single best method for such GHG emission quantification, as every approach fits a certain spatial and temporal scale of interest and requires specific data to exist, mostly atmospheric GHG concentrations and the wind field. While bottom-up approaches sum or extrapolate direct or indirect emission measurements at known sources, top-down methods use amospheric measurements to estimate the total emitted amount over an area [7,8]. Bottom-up and top-down estimates can differ

The equipment was largely financed by the Alfred-Teufel Foundation. The funders had no role in study design, data collection and analysis, decision to publish, or preparation of the manuscript.

Competing interests: The authors have declared that no competing interests exist.

significantly, with bottom-up being known for yielding lower total emissions because not all sources are known or their emissions being underreported [9,10]. If however the sources are known precisely, bottom-up estimates directly at their locations are more accurate, although their temporal resolution and long-term consistency are often lacking [11].

There exist several top-down trace gas emission quantification methods. As the transport of a trace gas in the atmosphere is governed by the equation of continuity, Fick's laws of diffusion, and ultimately the Navier-Stokes equations, common approaches for GHG emission quantification and source location are based on these physical laws, combinations or simplifications of them. Solving these equations numerically is done with Eularian atmospheric models such as ICON [12], PALM [13], MITRAS [14,15] and many others depending on the scale and complexity of interest. Provided initial and boundary conditions, preparatory work and significant computational resources, these eventually yield continuous fields of wind vector and potentially also trace gas concentrations for the simulated domain. This presents a versatile base for a variety of emission quantification schemes, most prominently inverse modelling by either solving a linear relationship between sources in the model and observations [16] or by simulating backwards transport of (an ensemble of) particles from observation points back to the sources. Examples of the latter are the inverse Lagrangian transport models HYSPLIT [17], STILT [18] and FLEXPART [19], which differ for example in their stochastic representation of turbulence.

In case no continuous Eularian model output is available, relying exclusively on measurements is possible for example by solving the Advection-Diffusion Equation (ADE) [20]. If numerical solving is unviable, common simplified analytical solutions of the ADE are the Gaussian plume or puff equation [20], which allow for quick simulation of concentration profiles or time series given meteorological conditions such as wind and atmospheric stability. Fitting a Gaussian plume or puff to concentration measurements with large, distinct peaks from emission events then give an estimate on the emitted mass of gas.

An even more rudimentary approach (often referred to as "mass balance approach") is based on the divergence theorem, where fluxes through a boundary around an emission hotspot are parametrised through wind and concentration measurements and then integrated to estimate the mass flow at the hotspot [21], potentially in combination with a Gaussian puff model [22]. A particular in-situ measurement type that provides both wind, concentrations, and gas flux data is the eddy covariance (EC) method, where fast measurements of the wind vector are correlated with fast trace gas concentration fluctuations to measure the turbulent transport by eddies directly [23]. While the quality of EC measurements is high, equipment is expensive, and the theory is difficult to apply in complex terrain or for inhomogeneous emissions [24] as the footprint of this single-point measurement depends heavily on the atmospheric conditions, raising representativeness concerns [25]. Furthermore, the standard EC method aims to quantify *vertical turbulent* gas transport resulting from the interplay of concentration and wind fluctuations and specifically neglects *horizontal* or *advective* fluxes with the mean wind, which might be very relevant depending on the site.

All of the above methods require knowledge of the wind vector, either by simulation, measurements, or assumptions. Furthermore, it is implicitly assumed that the trace gas of interest is transported directly with this wind vector. If for a GHG emitting site the prerequisites for the none above methods are satisfyingly fulfilled, custom solutions need to be developed. This can be the case for emission sites well in the meteorological microscale (spatial scale below 1 km) with heterogeneous emissions, and/or in complex terrain with intricate slope flows, heavy vegetation or small-scale features that reduce representativeness of wind measurements. The Starzach site, a site near the eastern slope of the Black Forest with natural, non-volcanic, magmatic CO_2 emissions from mofettes [26], falls into this category.

In the following, we present a top-down method for quantifying the CO_2 emissions at the Starzach site, based solely on CO_2 point measurement time series at irregular locations with no wind vector required. We cross-correlate sensor time series to reconstruct the near-surface CO_2 movement vector field, then apply the divergence theorem during situations of low vertical mixing to integrate the total emitted CO_2 flux over the area. The results are compared to previous bottom-up estimates and a Gaussian puff model approach.

Materials and methods

The Starzach site

The upper Neckar river valley east of the Black Forest in southern Germany is known for its natural CO_2 emissions of non-volcanic, magmatic origin [26]. During the 20th century, CO_2 gas was mined industrially in the area until yields eventually declined drastically, so that after around 100 years, practically no CO_2 exhaust was observable anymore [26]. In the 1980s, at the peak of active industrial extraction, individual wells in the Neckar valley, for which data exists, typically extracted 1000–4000 $\mathrm{t\,yr^{-1}}$ (2800–11,000 $\mathrm{kg\,d^{-1}}$) of CO_2, mostly by actively lowering the groundwater level with pumps to ease gas uprise [26]. The Starzach site is one of these extraction sites, located at a northern slope in the Neckar valley, with orographic structures, vegetation and trees far smaller than the resolution of common global circulation models (GCMs) or reanalyses datasets. To the authors' knowledge, no tailored wind field simulations exist for this region. Focused points of CO_2 exhalation (mofettes) with diameters up to 30 cm are scattered across the site, primarily along a north-westerly line, where a geological fault is suspected [26,27]. The main mofette area of interest in this analysis (Fig 1) has an extent of 20 m $\times$ 20 m. Over the 20 years after the termination of CO_2 mining, mofette activity gradually returned. In 2015, the mofette that was most prominent at the time was measured to emit around 75 $\mathrm{kg\,d^{-1}}$ [29]. A three meter deep groundwater well that was added in 2014 has since transformed into the site's most active mofette, for which direct measurements yielded average emission rates of 465 $\mathrm{kg\,d^{-1}}$ in winter 2022 [28], and roughly 520 $\mathrm{kg\,d^{-1}}$ in summer 2023 [30]. All these post-mining bottom-up measurements were performed by direct quantification of CO_2 exhaust with gas funneling systems, but different equipment. They suggest an overall trend of increasing CO_2 emissions at the site over the years and a possible seasonal cycle due to variable groundwater levels. Judging from the previous measurements, the amount and visual activity of the mofettes in the core Starzach mofette area (Fig 1), a rough estimate of 1500 $\mathrm{kg\,d^{-1}}$ of total emissions exclusively from individually identified mofettes can be made.

As CO_2 gas is nearly twice as dense as air under standard atmospheric conditions, it tends to flow or settle at the ground. This is visually evident for example in *Plate 4* of [31] from a smoke bomb plume following the terrain together with CO_2 from a gas vent in Italy, and an ice trail emerging from a Starzach mofette during winter in *Fig 2b* of [27]. Consequently, quantification efforts of the CO_2 emissions in Starzach must take this low-level horizontal gas flow into account by measuring close to the ground. Notably, the typical meteorological wind measurements in 2 m height above ground can not be used as a reliable proxy for near-surface CO_2 movements. Furthermore, classic eddy covariance measurements of the *vertical turbulent* CO_2 flux would be expected to dramatically underestimate the total emissions.

Starting in 2018, a low-cost near-surface CO_2 sensor network (Sensirion SCD30) and other meteorological equipment has been gradually deployed there for testing of different configurations and sensors [27], revealing a distinct diurnal pattern of wind direction due to the valley orography and very low wind speeds at night. This inhibits mixing and removal

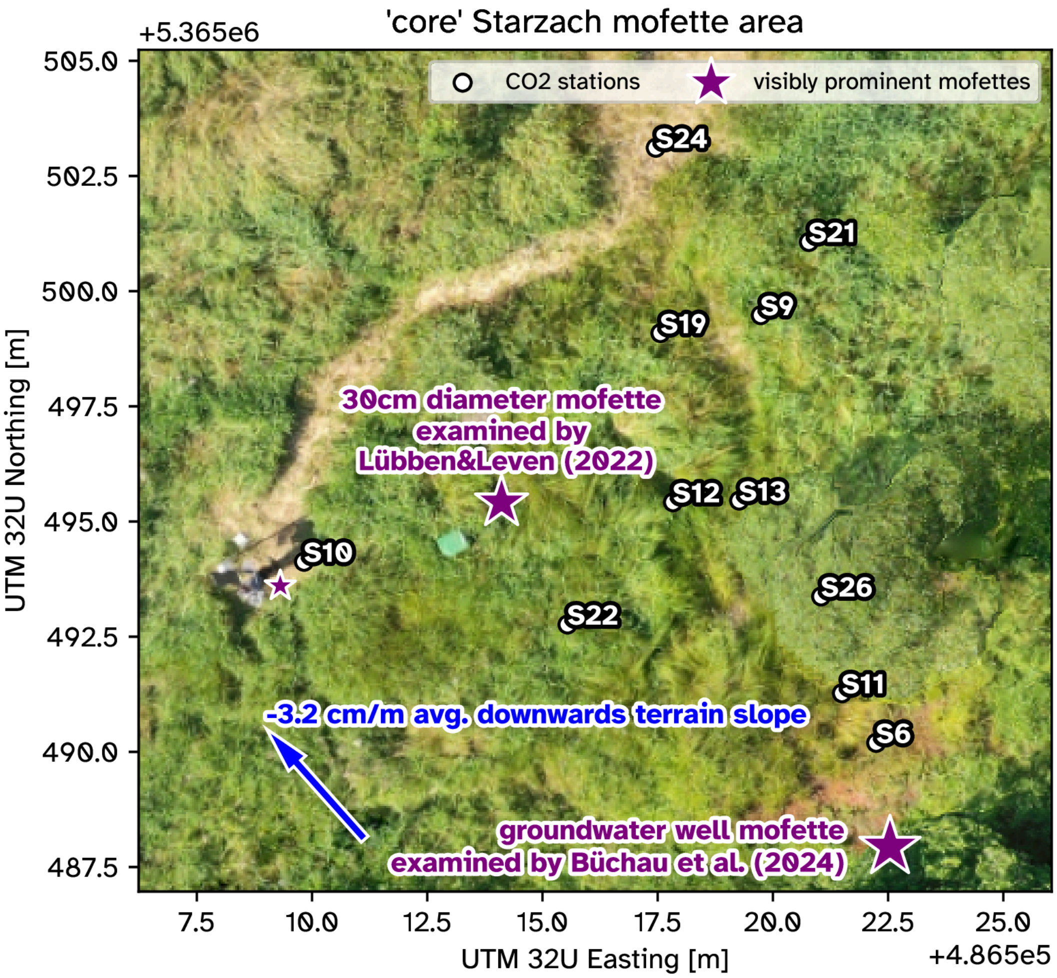

Fig 1. **The Starzach site's main mofette area.** Axes are in Universal Transverse Mercator (UTM) coordinates, offset from a value indicated at the upper end of each axis to keep numbers concise. Background picture taken by Martin Schön through aerial imaging in 2019. Purple stars indicate the visibly most active mofettes. Smaller mofettes and diffuse degassing area are not shown. The labels S6 through S26 indicate the positions of individual CO_2 monitoring stations. For a broader overview of the site and measurement system we refer to our previous publications [27,28].

https://doi.org/10.1371/journal.pclm.0000741.g001

of CO_2 and thus causes a significant diurnal cycle of near-surface atmospheric CO_2 concentrations up to 40,000 ppm (4 vol%, a 100-fold increase over the average atmospheric concentration) at night [27]. Fig 2 shows a typical diurnal near-surface CO_2 time series at 30 cm above ground with peak analysis. Stations are equipped with Sensirion SCD30 CO_2 sensors queried with the fastest measurement interval of two seconds. The stations usually observe around 1000 CO_2 concentration peaks (i.e. local maxima) per day, recurring in intervals of ten seconds up to a few minutes, and shorter peak durations of a few seconds up to a few minutes. During the day, peaks are slightly more frequent and shorter than during nighttime, while peak magnitude is mostly independent of time. Previous studies have shown, that the CO_2 degassing of an individual Starzach mofette does not exhibit any diurnal pattern [28,29], so this temporal difference can be explained with increased atmospheric mixing at daytime. Peak duration and intervals have a similar magnitude, which often causes significant overlap between peak flanks. Together with the high number of individual peaks, this complicates their isolation for fitting of Gaussian puffs or solving the ADE directly. Other gas emission quantification studies, like detection of industrial methane leaks or ship emissions with comparable release rates as the Starzach site at

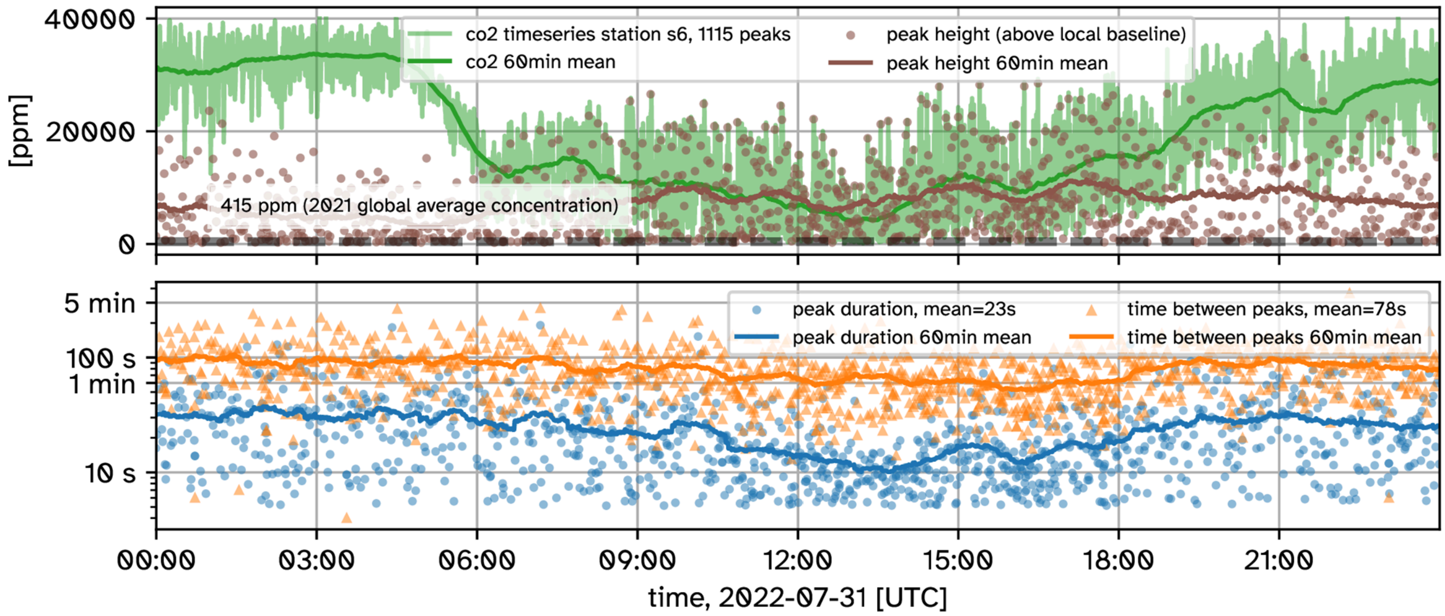

Fig 2. Typical 24 hour time series of a near-surface CO_2 station 6 at the Starzach site's main mofette area with global average CO_2 concentration reference of 415 ppm [2] (top), and peak duration and time between peaks (bottom).

https://doi.org/10.1371/journal.pclm.0000741.g002

an order of magnitude of $1000\,\mathrm{kg\,d^{-1}} \approx 40\,\mathrm{kg\,h^{-1}}$, typically fit Gaussian puffs or plumes to time series with 1–100 daily peaks (or "events") [32–34]. This is a lot less than in the present Starzach data (Fig 2) and consequently results in much reduced or no peak overlap – often a requirement for peak detection above a certain baseline and subsequent fitting. In fact, Gaussian puffs are generally used to quantify individual and separate release events, not a mostly continuous stream of gas emissions with only intermittent interruptions as found at the Starzach site.

CO_2 movement tracking

With no representative near-surface wind vector field available to parametrise CO_2 movement, we opted for a statistical approach as a proxy. The CO_2 concentration time series exhibit a large amount of local maxima (Fig 2), of which distinct patterns are often recognisable between neighbouring stations A and B at positions $\vec{p}_A$[m] and $\vec{p}_B$[m] respectively. The time shift Δt_{AB}[s] between these matching peak patterns is a function of time t[s] and a proxy for the duration it takes a packet of CO_2 to move from station A to station B. With the distance vector $\vec{d}_{AB}[\mathrm{m}] = \vec{p}_B - \vec{p}_A$ pointing from station A to station B, an estimate for the CO_2 movement speed vector $\vec{u}_{AB}$[m s^{-1}] can be derived:

$$\vec{u}_{AB}(t) = \frac{\vec{d}_{AB}}{\Delta t_{AB}(t)} \tag{1}$$

To calculate Δt_{AB}, we apply a 10 min-rolling window to each station combination pair. In this window, we determine the best-matching time shift from the maximum of the cross-correlation function of the two stations' CO_2 concentration time series. Each station in the sensor network delivers CO_2 concentration data roughly every two seconds, which is the sensor's fastest measurement rate. We resampled and interpolated all individual station data to one-second intervals for a common time resolution, so this rolling cross-correlation yields best-matching time shifts Δt_{AB} and the respective correlation values R_{AB}[1] at a rate of 1 Hz, which are shown in Figs 3 and 4 for an exemplary day (31.07.2022) and station

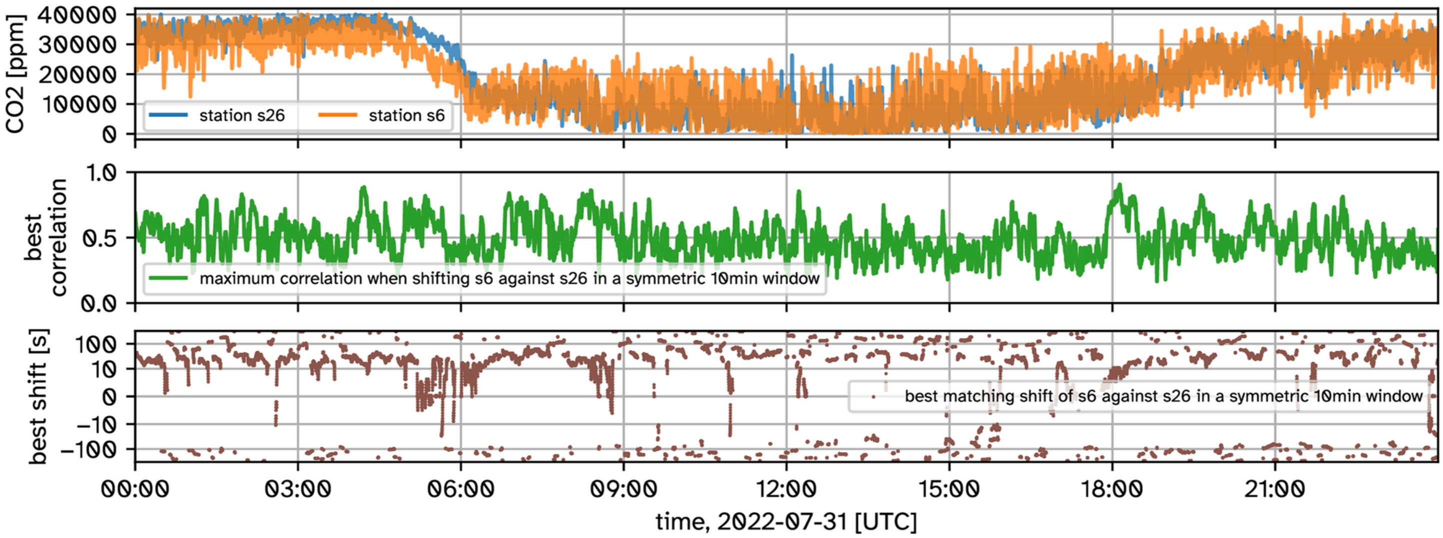

Fig 3. Time series of CO_2 concentration, best cross-correlation and shift of two stations at the Starzach site. Time series of station 6 and station 26 (top) are cross-correlated in a 10 min rolling window to determine the shift between them (bottom) from the highest cross-correlation value (center). In the lowest panel, the y-axis has a symmetric logarithmic scale, but the region −10 to 10 s is scaled linearly. See Fig 4 for a zoomed view.

https://doi.org/10.1371/journal.pclm.0000741.g003

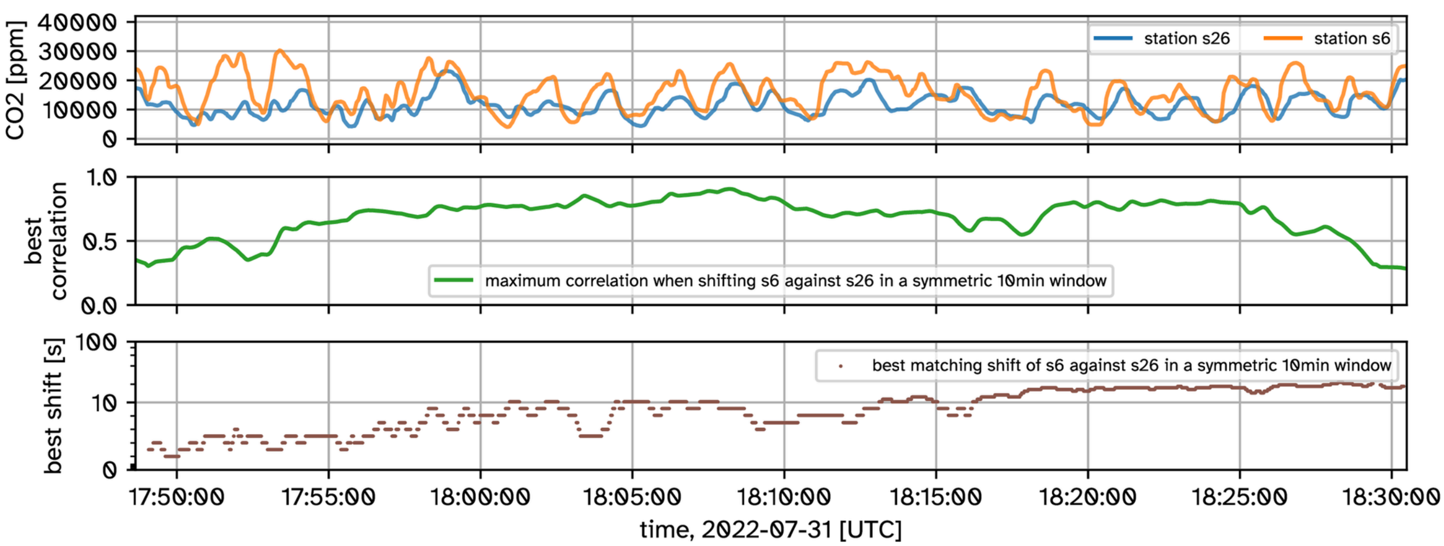

Fig 4. Zoomed view of Fig 3. A *positive* shift in the lowest panel means that the time series of of station **s6** needs to be moved *forward in time* (into the future) to match the time series of station **s26**.

https://doi.org/10.1371/journal.pclm.0000741.g004

pair (stations 6 and 26). The window size of 10 min was chosen, so enough surrounding peaks provide context for the cross-correlation to be meaningful. In other setups, this window size might need adjustment.

The magnitude of correlation between two stations varies significantly and covers the entire range from 0–100% (Figs 2 and 5). For this examined day, the stations closest to the central mofette have the highest correlations with each other, while stations from opposites sides of the area expectedly correlate poorly. The raw values of Δt_{AB} can jump erratically when there is a change in peak patterns that causes the cross-correlation to be numerically larger for a shift of opposite

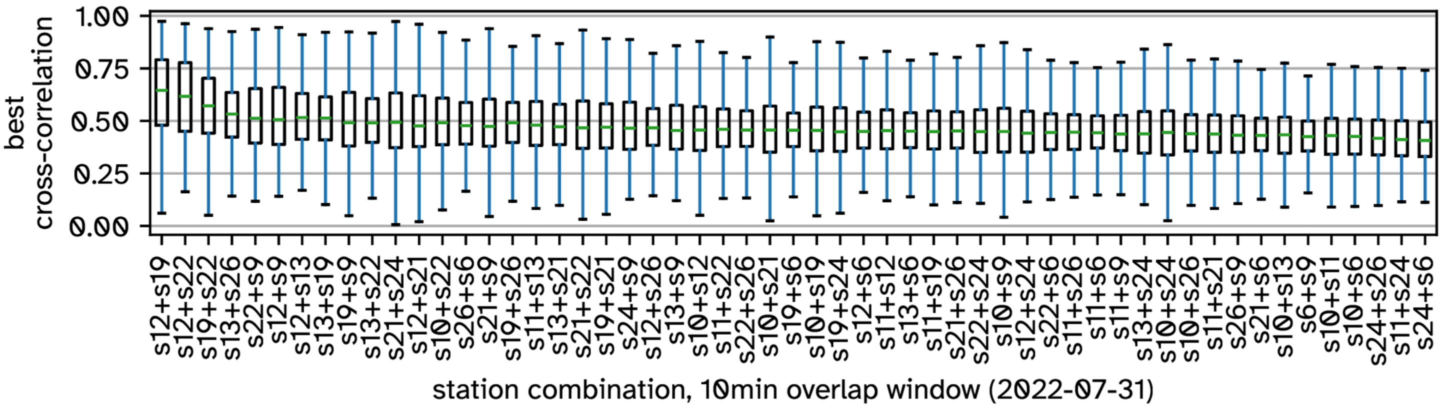

Fig 5. Boxplots of the best cross-correlation R_{AB} between CO_2 time series during one day (31.07.2022).

https://doi.org/10.1371/journal.pclm.0000741.g005

sign (Fig 3). When the overall level of correlation is high, this happens less or not at all (Fig 4). To extract a more robust estimate of time shift Δt_{AB} between stations, another 10 min rolling average was applied, weighted with the best cross-correlation R_{AB} raised to a power of six to filter out low correlation values.

Applying Eq (1), this rolling cross-correlation now contains CO_2 movement speed information on any line connecting a pair of stations. To map this irregularly distributed $\vec{u}_{AB}$ data onto a regular grid, we perform a weighted average, so the final CO_2 movement speed estimate $\vec{u}_{CO_2}$[m s^{-1}] in a grid cell center at location $\vec{p}$[m] is an average of all available $\vec{u}_{AB}$ estimates:

$$\underbrace{\vec{u}_{CO_2}(t,\vec{p})}_{CO_2 \text{ speed estimate}} = \underbrace{\frac{\sum_{AB} w_{AB}(t,\vec{p}) \cdot \vec{u}_{AB}(t)}{\sum_{AB} w_{AB}(t,\vec{p})}}_{\text{weighted average of all speed estimates}} \tag{2}$$

with the following weight w_{AB} [1]:

$$\underbrace{w_{AB}(t,\vec{p})}_{CO_2 \text{ speed weight}} = \underbrace{(R_{AB}(t))^3}_{\text{best correlation}} \cdot \underbrace{\exp\left(-\frac{\mathrm{sdf}_{AB}(\vec{p})}{5\,\mathrm{m}}\right)}_{\text{distance to both stations}} \cdot \underbrace{\exp\left(-\frac{\left|\vec{d}_{AB}\right|}{1\,\mathrm{m}}\right)}_{\text{distance between stations}} \tag{3}$$

where $\mathrm{sdf}_{AB}(\vec{p})$[m] is the closest distance of point $\vec{p}$ to the line segment connecting station A and B, also known as the *signed distance function* [35]. The weight w_{AB} ensures that *highly-correlated*, *close* neighbours, in the *near vicinity* are prioritised. The arbitrary normalisations of the individual factors of Eq (3) were chosen in accordance with the extents of its input variables and might need adjustments in a different setup. The product of CO_2 movement speed and mass concentration C_{CO_2}[kg m^{-3}] then yields the CO_2 mass transport or flux $\vec{F}_{CO_2}$[kg m^{-2}s^{-1}]:

$$\vec{F}_{CO_2}(t,\vec{p}) = \vec{u}_{CO_2}(t,\vec{p}) \cdot C_{CO_2}(t,\vec{p}) \tag{4}$$

Similar to $\vec{u}_{CO_2}$, for C_{CO_2} we average all concentration measurements weighted with the exponentially decaying distance to the respective station and a decay length of 1 m to inter- or extrapolate it to any location $\vec{p}$.

This presented cross-correlation method of estimating gas transports is inherently independent of spatial dimensionality, so it can be applied in one, two or three dimensions. In our case, we only have CO_2 data available in 30 cm height above ground, so we use a two-dimensional grid. In theory, $\vec{F}_{CO_2}$ can now be integrated over an arbitrarily-chosen boundary of interest ("mass balance approach") to determine the total flow of CO_2 $\dot{m}_{CO_2}$[kg s^{-1}] out of the region. However, unless this boundary is placed *between* stations, which dramatically restricts the total possible area and is thus wasteful, the representativeness of $\vec{F}_{CO_2}$ at the exact boundary can be doubted. Furthermore, all other arguably more representative data *inside* the volume of interest is ignored. So instead, we employ Gauss' divergence theorem [36], which allows to substitute the surface-integral over the boundary S[m^2] with a volume-integral over the divergence:

$$\underbrace{\dot{m}_{CO_2}}_{\text{emission rate}} = \underbrace{\int_S \vec{F}_{CO_2}(t,\vec{p})dS}_{\text{mass flow through boundary}} = \underbrace{\int_V \nabla \cdot \vec{F}_{CO_2}(t,\vec{p})dV}_{\text{mass emergence within boundary}} \tag{5}$$

This emission rate $\dot{m}_{CO_2}$ can then be integrated over a time frame of interest, such as one day, to calculate the total emitted mass of CO_2.

Verification with Gaussian Puff model

To verify the CO_2 emission rate $\dot{m}_{CO_2}$ derived with Eq (5), we use the well-established Gaussian puff method to simulate CO_2 transport from a mofette to a sensor station. This requires selecting one of the many available Gaussian puff equations and parametrisations, which is physically sensible and appropriate for fitting to observed Starzach CO_2 time series. We start with the Gaussian puff equation for the concentration $C[\mathrm{kg\,m^{-3}}]$ with reflection at the ground and no wind shear [20,37]:

$$C(t,x,y,z) = \frac{\sqrt{2}m}{4\pi^{\frac{3}{2}}\sigma_x\sigma_y\sigma_z}\left(e^{-\frac{(z+z_0)^2}{2\sigma_z^2}} + e^{-\frac{(z-z_0)^2}{2\sigma_z^2}}\right)e^{-\frac{y^2}{2\sigma_y^2}-\frac{(-tu+x)^2}{2\sigma_x^2}} \tag{6}$$

where $m[\mathrm{kg}]$ is the instantaneously emitted mass, $t[\mathrm{s}]$ the time since the emission event, $x[\mathrm{m}]$ the downwind distance, $y[\mathrm{m}]$ the crosswind distance, $z[\mathrm{m}]$ the height above flat ground, $z_0[\mathrm{m}]$ the height of the emission source and $\sigma_x, \sigma_y, \sigma_z[\mathrm{m}]$ the puff spreads in the respective spatial directions. In this form, with constant puff spreads σ_i, an emitted packet of CO_2 moves with invariable speed and shape. While this Eq (6) is a physical solution of the advection-diffusion equation, constant puff spreads σ_i are unrealistic - a puff's extent *does* change gradually after its release [38]. It is thus common to parametrise the spreads σ_i with monotonic functions such as a power-law or a function that can be approximated by a power-law, either in terms of time t [38–41]:

$$\sigma_i(t) = a_i t^{b_i} \ \left(\text{units: } [\sigma_i] = \mathrm{m},\ [t] = \mathrm{s},\ [a_i] = \mathrm{ms}^{-b_i},\ [b_i] = 1\right) \tag{7}$$

or in terms of downwind distance x [34,42–44]:

$$\sigma_i(x) = a_i x^{b_i} \ (\text{units: } [\sigma_i] = \mathrm{m},\ [a_i] = \mathrm{m},\ [x] = \mathrm{m},\ [b_i] = 1) \tag{8}$$

Despite the original parametrisation being in terms of time t when the Gaussian puff model was introduced nearly a century ago [45], parametrisation in terms of downwind distance x have been more widely established - presumably because x is easier to quantify than travel time t. Therefore, several empirical tabular and graphical charts for parametrisations of puff spreads in terms of downwind distance x exist [46,47]. Due to the occurrences of the σ_i in Eq (6), these two parametrisations result in drastic differences in the simulated puff shape in space and time, and for the fulfillment of mass conservation. These differences are summarised in Table 1.

Mass conservation: Integrating the concentration over the entire spatial domain of a Gaussian puff yields the total distributed mass $m_{tot}[\mathrm{kg}]$, which should amount to the initially emitted mass m if mass conservation is fulfilled. In the case of Eq (6), this reads:

Table 1. Qualitative comparison of Gaussian puff spread σ_i parametrisations in terms of time or distance, based on with realistic (i.e. physically sensible or for Starzach data well-matching) and unphysical properties marked with color.

Parametr. →	with time: $\sigma_i(t) = a_i t^{b_i}$	with distance: $\sigma_i(x) = a_i x^{b_i}$
mass conservation	fulfilled	fulfilled for $b_x \leq \frac{1}{2}$ initial overestimation* for $\frac{1}{2} < b_x < 1$ not fulfilled for $b_x \geq 1$
peak shape in distance x	symmetric, Gaussian	asymmetric, "backward-leaning" (steep increase, shallow decrease)
peak shape in time t	asymmetric, "backward-leaning" (quick increase, slow decrease)	symmetric, Gaussian
peak movement	with speed u, everywhere	variable speed and mostly $\neq \frac{x}{t}$, artifacts with backwards-moving peak when off-axis ($\lvert y\rvert > 0$) and $b_i > \frac{1}{2}$
peak arrival time	different everywhere and mostly $\neq \frac{x}{u}$, artifacts where peak can arrive earlier downstream than upstream when off-axis ($\lvert y\rvert > 0$) with $b_i > \frac{1}{2}$	with speed u, $t_{\text{peak}} = \frac{x}{u}$ i.e. peak arrives as "wall" everywhere

*only $x > 0$ can be considered in Eq (9) here, so there is an initial phase where $50\% \leq \frac{m_{\text{tot}}}{m} \leq 100\%$, because diffusion in the backwards direction causes matter to be present at $x < 0$, thus not contributing to m_{tot}.

https://doi.org/10.1371/journal.pclm.0000741.t001

$$m_{\text{tot}} = \int_0^\infty \int_{-\infty}^\infty \int_{-\infty}^\infty C(t,x,y,z)\, dx\, dy\, dz \overset{\substack{\text{mass}\\ \text{conservation}}}{\overset{!}{=}} m \tag{9}$$

For time-based σ_i parametrisation, the emitted puff mass is always conserved. Distance-based σ_i parametrisation on the other hand only eventually ($t \to \infty$) conserves mass for moderate mixing along the direction of flow ($b_x < 1$), but linear or superlinear longitudinal spreading ($b_x \geq 1$) violates mass conservation, as it is too far from the actual physical solution, which is $b_i = 0$ or $\sigma_i = \text{const}$.

Peak shape: Whether t or x is present in the demoninator of Eq (6) controls the peak shape in space and time. Eq (6) does not include wind shear, a process that influences mixing and thus puff shape. Taking wind shear into account results in a slightly "forward-leaning" concentration profile along the wind shear direction [48]. Due to an accumulation of the trace gas at the front of the puff, this can be considered more realistic than plain symmetric Gaussian or asymmetric "backwards-leaning" (steep increase, shallow decrease) peak shapes as predicted by the respective σ_i parametrisation of Eq (6). Wind speeds at the Starzach site are already very low (section The Starzach site) and we do not have vertical wind profile information, so we neglect the numerically probably small wind shear for simulating Gaussian puffs.

Peak movement: Where the two σ_i parametrisations differ significantly is peak movement speed and arrival time, two important quantities in our CO_2 movement tracking method described in section *CO_2 Movement Tracking*. The downwind peak position $x_{\text{peak}}[\text{m}]$ can be determined from the concentration maximum in x of Eq (6) analytically, i.e. solving $\frac{\partial}{\partial x} C(t,x,y,z) = 0$ for x. Analogously, peak arrival time $t_{\text{peak}}[\text{s}]$ is found by solving $\frac{\partial}{\partial t} C(t,x,y,z) = 0$ for t. Counterintuitively, due to the nature of the chosen empirical parametrisations, these do not exclusively turn out as simple functions of the wind speed u, especially in the early phase of emission: Having the puff spread $\sigma_i(x)$ depend on distance results in variable peak speed and introduces artifacts where off-axis peaks can even move *backwards* temporarily when $b_x > \frac{1}{2}$. In addition, peaks arrive after time $t_{\text{peak}} = \frac{x}{u}$ regardless of lateral position y, which is unrealistic. On the other hand, with $\sigma_i(t)$ parametrisation, the CO_2 peaks move at a constant speed u regardless of location and peak arrival time increases with lateral distance y. Still, similar artifacts exist when $b_x > \frac{1}{2}$. So in conclusion, to minimize unphysical puff behaviour and for simplicity, we continue with $\sigma_i(t)$ parametrisation, $b_i = \frac{1}{2}$, $y = 0$, and $z_0 = 0$, because the mofettes emit at ground level:

$$C_{\text{sqrt-simple}}(t,x,z) = \frac{\sqrt{2}m}{2\pi^{\frac{3}{2}} a_x a_y a_z t^{\frac{3}{2}}} e^{-\frac{z^2}{2a_z^2 t} - \frac{(-tu+x)^2}{2a_x^2 t}} \tag{10}$$

Puffs expanding proportionally to the square root of elapsed time is also supported by [38,39], especially in the early phase after emission, which we are interested in here. To estimate a CO_2 mass emission rate $\dot{m}_{CO_2}$ with Eq (10), we choose a station in a time frame where it is evidently in line with the general movement direction of CO_2 emerging from a specific mofette and fit a summed series of Gaussian puffs to the concentration time series. Setting $y = 0$ is thus reasonable, and without information about lateral diffusion, we furthermore assume it equals longitudinal diffusion: $a_x = a_y$. The total of the fitted Gaussian puff masses $\sum m$ divided by the time frame is then an estimate of $\dot{m}_{CO_2}$ and can be compared to the results from Eq (5).

Results

For consistency, most figures in this paper depict data from the 31.07.2022, which we use as a demonstration day for our methods. The data we used is available at [49]. Fig 6 shows a time snapshot of the CO_2 transport vector $\vec{F}_{CO_2}$

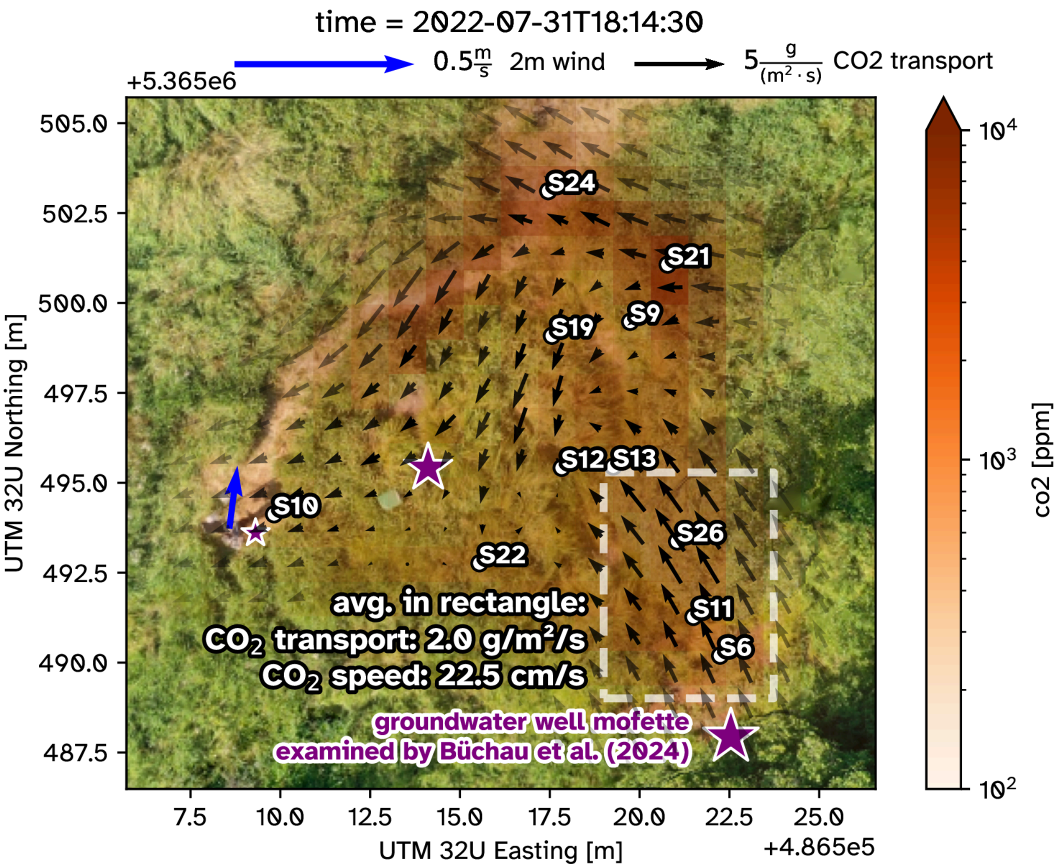

Fig 6. Snapshot of CO_2 transport vector field at the Starzach site in July 2022, derived from cross-correlations between concentration time series according to Eq (5) on a horizontal grid with 1 m resolution. To emphasize real data availability, the black CO_2 transport arrows' opacity is scaled with the smallest $\text{sdf}_{AB}(\vec{p})$, i.e. the closest distance to any station-connecting line segment. The purple stars indicate the visibly most prominent mofettes as in Fig 1. The white rectangle indicates the region used for the top graph in Fig 7 and as a reference in Fig 9.

https://doi.org/10.1371/journal.pclm.0000741.g006

calculated from Eq (4) in the early evening. At this time, sun is already blocked from reaching the site due to the hillslope in the south, leaving mostly very slow downslope northwards winds [27], in this case a practically negligible 2 m wind speed below $0.2\,\mathrm{m\,s^{-1}}$. The emitted CO_2 is thus not advected with the wind, but can instead flow along the terrain due to its higher density [31]. This is particularly evident in the white marked rectangle in Fig 6, where $\vec{F}_{CO_2}$ resulting from CO_2 exhaust of the groundwater well clearly follows the general direction of the terrain gradient (Fig 1).

The lack of vertically resolved information requires an assumption of integration height in the volume integral of Eq (5), for which we choose one meter. The mofettes emit nearly 100 vol% CO_2 [26,28,29], which under calm conditions mostly accumulates near the surface. At 30 cm height, where our sensors are mounted, the highest recorded concentrations are around 4 vol%, so it should be safe to assume that the CO_2 concentration at 1 m height becomes negligible for Eq (5).

As can be seen from the black $\vec{F}_{CO_2}$ arrows in Fig 6, positive divergence (i.e. acceleration or radially pointing away from a specific location) is not exclusively the predominant pattern - negative divergence (i.e. convergence, deceleration or arrows pointing towards each other) does also occur. Positive divergence results from introduction of CO_2 from the site's sources into our chosen boundary, negative divergence from removal. The contribution of the vegetation through photosynthesis can be neglected, as it is three orders of magnitude smaller than the mofettes' exhaust [27]. Instead, we attribute the presence of negative divergence to the fact that we only have horizontal information in the plane 30 cm above ground, and CO_2 can escape out of this plane by moving vertically. The argument can be made that once a packet of CO_2 has moved downwards, it will most likely stay close to the ground due to its higher density. Conversely, if vertical mixing by eddies causes CO_2 to be moved upwards, this individual packet of CO_2 will probably not re-enter our horizontal measurement plane either as it is mixed away. So to handle this, we do not categorically ignore immediate negative divergence, but instead clip negative values of the integrated mass rate $\dot{m}_{CO_2}$ to zero, to filter out situations with significant vertical movements out of our horizontal plane, which we would falsely count negatively towards the emission rate.

Fig 7 shows a time series of the estimated CO_2 mass rate $\dot{m}_{CO_2}$ integrated from the CO_2 transport divergence in Eq (5) with all previously motivated assumptions. From the very low estimated rates at daytime (06:00–18:00 UTC) it is evident that the aforementioned vertical mixing (by convection and turbulence) is too significant in this time frame for our two-dimensional method to be reliable. However, at night (18:00–06:00 UTC) the average rate downstream of the groundwater well mofette matches its exhaust rate measured directly with a funnel system very well ($414.7\,\mathrm{kg\,d^{-1}}$ vs. $465\,\mathrm{kg\,d^{-1}}$) [28]. Another independent validation of this result comes from fitting a series of Gaussian puffs to the time series of station 6 (Fig 8), giving a result of $4.8\,\mathrm{g\,s^{-1}}$ that is equally well in line with the direct bottom-up measurement of $5.5\,\mathrm{g\,s^{-1}}$ [28]. The CO_2 flux in the white rectangle of Fig 6 averages to $2\,\mathrm{g\,m^{-2}\,s^{-1}}$, which also comes close to this result when assuming a reference area sized 1 m (our integration height as argued above) by 2.5 m, roughly corresponding to the width of the rectangle. Expanding the temporal scale to one and a half months, a standard deviation of 40% (Fig 9) is introduced. But the average of $517\,\mathrm{kg\,d^{-1}}$ matches the most recently measured groundwater well CO_2 exhaust of roughly $520\,\mathrm{kg\,d^{-1}}$ in summer 2023 very well [30]. Applied to the entire core Starzach mofette area as defined by Fig 1, the average total CO_2 emission is estimated to be $3266\,\mathrm{kg\,d^{-1}}\pm 42\%$. This range is comparable to available gas extraction data from a well one kilometer east of the Starzach site during industrial mining in the 1980s [26].

Discussion

The above results agree well with previous measurements and confirm that our design choices and assumptions are justified and sufficiently work around the method's limitations, which we discuss below. Interestingly, the result of $3266\,\mathrm{kg\,d^{-1}}\pm 42\%$ is twice as high as the rough estimate of mofette-only emissions with $1500\,\mathrm{kg\,d^{-1}}$ made in section *The Starzach site*. This suggests that non-mofette, invisible diffuse degassing plays a larger role than previously assumed.

Under calm conditions and on flat terrain, the ADE dictates that CO_2 emitted from a mofette diffuses radially outwards. Stations at comparable distances to a mofette such as station 12 and 22 thus experience similar fluctuations in their CO_2

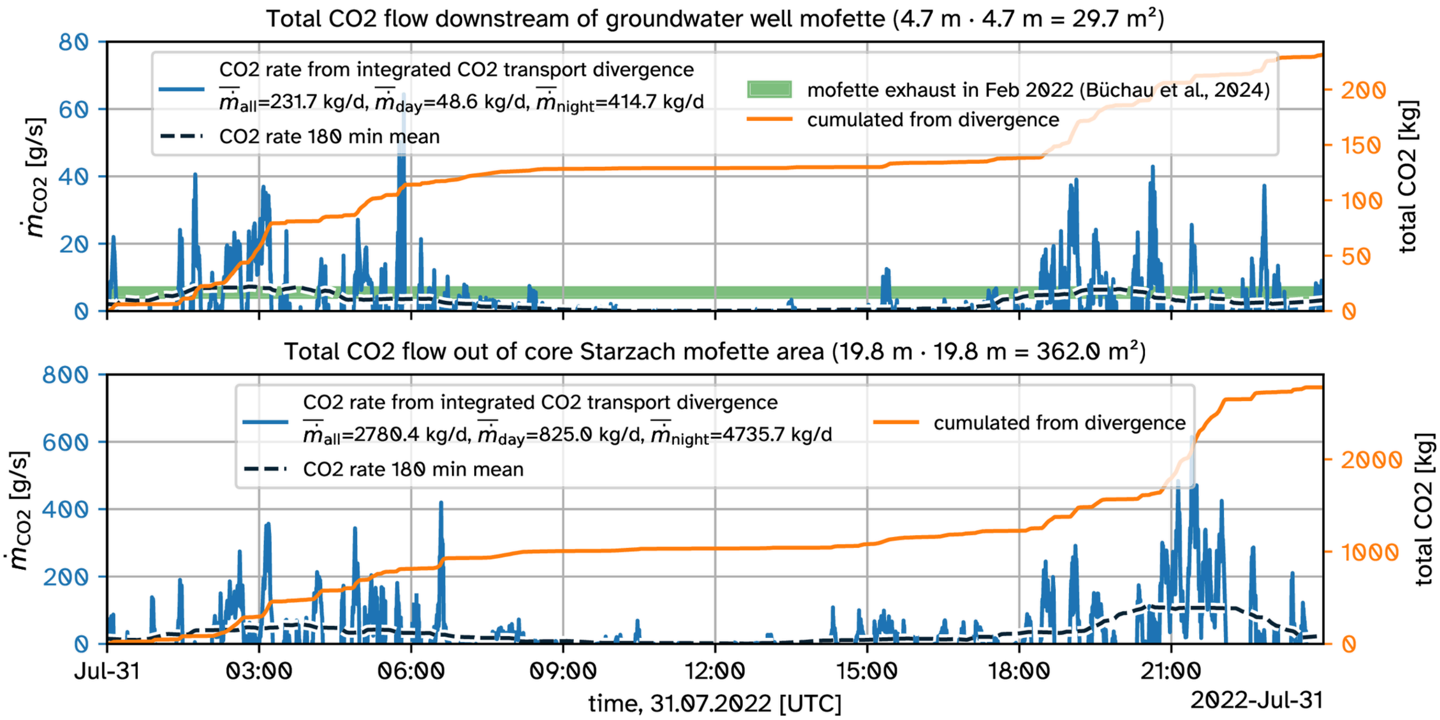

Fig 7. Time series of total CO_2 mass emission rate at the Starzach site, calculated from integrated CO_2 transport divergence according to Eq (5) for the white rectangle downstream fo the groundwater well mofette in Fig 6 (top) and the entire core Starzach mofette area (bottom). The mass rate averages $\overline{\dot{m}}$ in the legends are calculated for **all** data, **day**time (06:00–18:00 UTC) and **night**time (18:00–06:00 UTC).

https://doi.org/10.1371/journal.pclm.0000741.g007

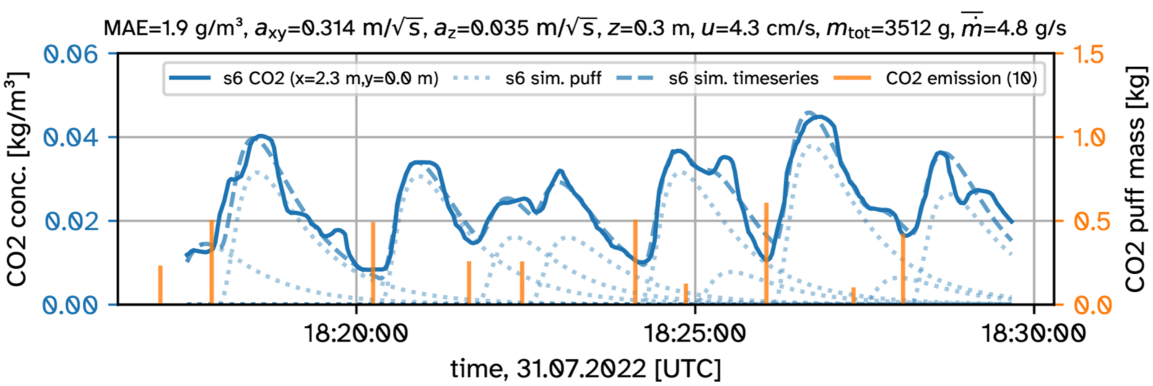

Fig 8. A series of Gaussian CO_2 puffs fitted to station 6 data based on Eq (10). Time and location match the white rectangle in Fig 6. Each individual simulated CO_2 puff of mass *m* (**orange** bars) contributes one peak (**blue** dotted lines) to the summed simulated time series (**blue** dashed line). Time shifts and masses for each puff and the parameters *u*, a_x(=a_y) and a_z of Eq (10) were optimized iteratively with methods available in SciPy [50] to best match the measured CO_2 time series of station 6 (**blue** solid line).

https://doi.org/10.1371/journal.pclm.0000741.g008

concentration time series, resulting in a high cross-correlation at only a small time shift between them (Fig 5). Our cross-correlation method based on Eq (2) then falsely interprets this as a fast movement *between* these stations. While this artifact does occur, it is apparently canceled out to a large degree when averaging long enough (Fig 9). A mitigation strategy could be to place stations *around* mofettes in at least two outer ring formations, so the radial movements can be observed

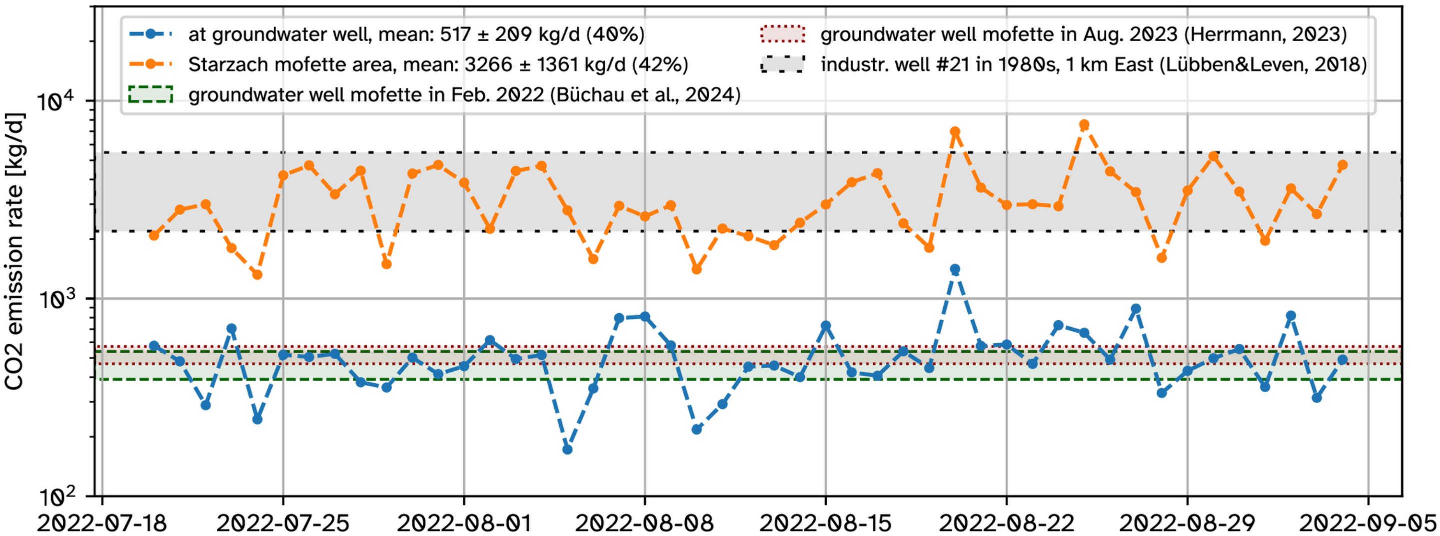

Fig 9. Average daily CO_2 emission rates at the Starzach site over 47 days. The **blue** and **orange** lines consist of the respective average CO_2 emission rates $\dot{m}_{CO_2}$ derived with Eq (5) in the night between 18:00 and 06:00 UTC as motivated by Fig 7.

https://doi.org/10.1371/journal.pclm.0000741.g009

properly. We thus attribute the rather high standard deviation of 40% for $\dot{m}_{CO_2}$ in Fig 9 mostly to a lack of spatial measurement density, and expect this spread to decrease when more sensor stations are used and especially the vertical distribution and movement of CO_2 is quantified.

An alternative gas movement tracking approach more robust against these artifacts would be to assume that an observed peak of CO_2 always originates from a radial movement away from a certain center point. A "dispersion circle" can then be fitted to three or more station's peak arrival times, directly yielding dispersion speed and origin. The ensemble of fitted circles would then also give a source location probability map to pinpoint emission hotspots. But this would introduce possibly non-deterministic iterative fitting as commonly done for Gaussian puff-based approaches [22,34], which our current method does not require.

Another noticeable observation is the discrepancy between mofette degassing periodicity (roughly every four seconds for the groundwater well [28]) and the significantly slower peak frequency (over one minute on average for station 6, Fig 2) in the sensor stations' CO_2 time series, and the simulated Gaussian puffs (Fig 8). While it is to be expected that downstream peak frequency reduces slightly with traveled distance due to mixing [51], an order of magnitude difference over such a short distance of a few meters can not be explained in this way. The time series patterns in Fig 4 might suggest a small-scale vertical atmospheric oscillation as the reason, periodically bringing CO_2-saturated air from below, then fresh air from above to the sensor. For a Brunt-Väisälä buoyancy frequency [52] ranging in the typical CO_2 peak recurrence time of 60–200 s (Fig 2), a very stable vertical potential temperature gradient of 0.03–0.3 $K\,m^{-1}$ very close to the ground/directly at the surface is required. This is reasonable, considering that the emitted CO_2 has a temperature between 8–14 °C [28,30], which in this case is colder than the surrounding air, enhancing atmospheric stability. Another possibility is that emitted CO_2 first accumulates around the source, its movement initially inhibited by vegetation and small-scale terrain features, until a threshold is overcome and a larger idealised packet of CO_2 begins flowing at once. This theory could also explain the significantly less frequent time series peaks. It is furthermore supported by the good agreement of the peak shapes in time (Fig 8, quick increase, slower decrease) with the Gaussian puff solution (Eq (10), Table 1), suggesting the movement of a connected mass of CO_2. Interestingly, the fitted Gaussian puff speed u (4.3 $cm\,s^{-1}$, Fig 8) is much smaller than the more realistic correlation-based speed (22.5 $cm\,s^{-1}$, Fig 6). We ascribe this to our negligence of wind shear in Eq (10), causing the Gaussian puff to be transported with a constant speed even directly at the surface, resulting in a lower fitted virtual transport speed u to match model to reality. In any case, simulation of the wind field and CO_2 movements at the Starzach site with a Eularian model could clarify the interdependence of mofette degassing periodicity and the slower measured fluctuations in atmospheric CO_2 concentration.

Conclusion

A top-down method was presented to derive CO_2 mass emission rates over an area, based solely on arbitrarily-positioned atmospheric concentration time series. No wind vector information is required as it is derived from cross-correlations between sensors. The method only requires iteration in form of rolling operations, which are deterministic, predictable in runtime and can be reduced in resolution to adjust performance, rendering it real-time applicable. As it only requires a mostly unstructured array of spatial gas concentration measurements, it presents a viable monitoring strategy for environments such as CCS sites, for which the Starzach site in south-western Germany has been proposed as a natural analog [26]. The method was validated with a low-cost sensor network at the Starzach site, a location featuring naturally occurring CO_2 emissions from mofettes, with previous individual bottom-up measurements and a Gaussian puff approach. An average total CO_2 emission rate of $3266\,\mathrm{kg\,d^{-1}} \pm 42\%$ was calculated over one and half months in late summer 2022 for the core Starzach mofette area, for which no such estimate has been available in the known literature until now. This result suggests that invisible, diffuse degassing at the site, which does not originate from visible mofettes, might be more significant than previously expected, and should be investigated further, for example with accumulation chambers. Furthermore, it demonstrates the viability of using low-cost sensors for gas emission quantification schemes: Data of only eleven commercially-available CO_2 sensors costing much less than 100 Euro each was used, together with an equally cost-effective infrastructure and automatic data collection strategy, which dramatically simplifies upscaling of spatial coverage. To reduce the result's uncertainty, the experiment should be repeated with a longer time frame and a higher special measurement density, notably with vertically resolved concentration measurements. Finally, the method should be compared to a Eularian model finely resolving the wind field and gas movements to confirm assumptions and results.

Acknowledgments

This work was supported by the German Research Foundation (DFG) under grant number BA 1988/19-1. The equipment was largely financed by the Alfred-Teufel Foundation. We thank Max-Richard Freiherr von Rassler for access to the field site and Björn Riebandt and Carsten Leven for their general support. We used PARMESAN for meteorological calculations [53], Sympy [54] for derivation, rearrangement and analysis of equations, SciPy [50] for fitting and other calculations and Matplotlib [55] for plotting.

Author contributions

Conceptualization: Yann Georg Büchau.

Data curation: Yann Georg Büchau.

Formal analysis: Yann Georg Büchau.

Funding acquisition: Jens Bange.

Investigation: Yann Georg Büchau.

Methodology: Yann Georg Büchau.

Project administration: Yann Georg Büchau.

Resources: Yann Georg Büchau.

Software: Yann Georg Büchau.

Supervision: Jens Bange.

Validation: Yann Georg Büchau.

Visualization: Yann Georg Büchau.

Writing – original draft: Yann Georg Büchau.

Writing – review & editing: Yann Georg Büchau, Jens Bange.

References

1. Filonchyk M, Peterson MP, Zhang L, Hurynovich V, He Y. Greenhouse gases emissions and global climate change: examining the influence of CO2, CH4, and N2O. Science of The Total Environment. 2024;935:173359. https://doi.org/10.1016/j.scitotenv.2024.173359
2. Calvin K, Dasgupta D, Krinner G, Mukherji A, Thorne PW, Trisos C, et al. Climate Change 2023: Synthesis Report. Geneva, Switzerland: Intergovernmental Panel on Climate Change (IPCC). 2023.
3. UNFCCC. The Paris Agreement. United Nations Framework Convention on Climate Change; 2015.
4. Gerbig C, Akinyede R, Custódio D, Gałkowski M, Ho D, Maier F. Steps towards improved inverse modelling of GHG fluxes: recent work within ITMS. In: Copernicus Meetings; 2025.
5. Harris SJ, Schwietzke S, France JL, Velandia Salinas N, Meixus Fernandez T, Randles C, et al. Methane emissions from the Nord Stream subsea pipeline leaks. Nature. 2025;637(8048):1124–30. https://doi.org/10.1038/s41586-024-08396-8
6. Munassar S, Rödenbeck C, Gałkowski M, Koch F-T, Totsche KU, Botía S, et al. To what extent does the CO2 diurnal cycle impact flux estimates derived from global and regional inversions?. Atmos Chem Phys. 2025;25(1):639–56. https://doi.org/10.5194/acp-25-639-2025
7. Nisbet E, Weiss R. Top-down versus bottom-up. Science. 2010;328(5983):1241–3. https://doi.org/10.1126/science.1189936
8. Janssens-Maenhout G, Petrescu AMR, Muntean M, Blujdea V. Verifying greenhouse gas emissions: methods to support international climate agreements. Greenhouse Gas Measurement and Management. 2011;1(2):132–3. https://doi.org/10.1080/20430779.2011.579358
9. Tejada G, Gatti LV, Basso LS, Cassol HLG, Silva-Junior CHL, Mataveli G, et al. CO2 emissions in the Amazon: are bottom-up estimates from land use and cover datasets consistent with top-down estimates based on atmospheric measurements?. Front For Glob Change. 2023;6. https://doi.org/10.3389/ffgc.2023.1107580
10. Sargent M, Barrera Y, Nehrkorn T, Hutyra LR, Gately CK, Jones T, et al. Anthropogenic and biogenic CO 2 fluxes in the Boston urban region. Proc Natl Acad Sci USA. 2018;115(29):7491–6. https://doi.org/10.1073/pnas.1803715115
11. Asefi-Najafabady S, Rayner PJ, Gurney KR, McRobert A, Song Y, Coltin K, et al. A multiyear, global gridded fossil fuel CO2 emission data product: Evaluation and analysis of results. JGR Atmospheres. 2014;119(17). https://doi.org/10.1002/2013jd021296
12. Zängl G, Reinert D, Rípodas P, Baldauf M. The ICON (ICOsahedral Non-hydrostatic) modelling framework of DWD and MPI-M: Description of the non-hydrostatic dynamical core. Quart J Royal Meteoro Soc. 2014;141(687):563–79. https://doi.org/10.1002/qj.2378
13. Maronga B, Banzhaf S, Burmeister C, Esch T, Forkel R, Fröhlich D, et al. Overview of the PALM model system 6.0. Geosci Model Dev. 2020;13(3):1335–72. https://doi.org/10.5194/gmd-13-1335-2020
14. Badeke R, Matthias V, Grawe D. Parameterizing the vertical downward dispersion of ship exhaust gas in the near field. Atmos Chem Phys. 2021;21(8):5935–51. https://doi.org/10.5194/acp-21-5935-2021
15. Grawe D, Schlünzen KH, Pascheke F. Comparison of results of an obstacle resolving microscale model with wind tunnel data. Atmospheric Environment. 2013;79:495–509. https://doi.org/10.1016/j.atmosenv.2013.06.039
16. Cho T, Chung J, Miller SM, Saibaba AK. Computationally efficient methods for large-scale atmospheric inverse modeling. Geosci Model Dev. 2022;15(14):5547–65. https://doi.org/10.5194/gmd-15-5547-2022
17. Draxler RR, Hess GD. An overview of the HYSPLIT_4 modelling system for trajectories. Australian Meteorological Magazine. 1998;47(4):295–308.
18. Lin JC, Gerbig C, Wofsy SC, Andrews AE, Daube BC, Davis KJ, et al. A near-field tool for simulating the upstream influence of atmospheric observations: The Stochastic Time-Inverted Lagrangian Transport (STILT) model. J Geophys Res. 2003;108(D16). https://doi.org/10.1029/2002jd003161
19. Pisso I, Sollum E, Grythe H, Kristiansen NI, Cassiani M, Eckhardt S, et al. The Lagrangian particle dispersion model FLEXPART version 10.4. Geosci Model Dev. 2019;12(12):4955–97. https://doi.org/10.5194/gmd-12-4955-2019
20. Stockie JM. The mathematics of atmospheric dispersion modeling. SIAM Rev. 2011;53(2):349–72. https://doi.org/10.1137/10080991x
21. Karion A, Sweeney C, Pétron G, Frost G, Michael Hardesty R, Kofler J, et al. Methane emissions estimate from airborne measurements over a western United States natural gas field. Geophysical Research Letters. 2013;40(16):4393–7. https://doi.org/10.1002/grl.50811

22. Daniels WS, Jia M, Hammerling DM. Detection, localization, and quantification of single-source methane emissions on oil and gas production sites using point-in-space continuous monitoring systems. Elem Sci Anth. 2024;12(1). https://doi.org/10.1525/elementa.2023.00110
23. Foken T. Springer handbook of atmospheric measurements. Cham: Springer; 2021.
24. Baldocchi DD. Assessing the eddy covariance technique for evaluating carbon dioxide exchange rates of ecosystems: past, present and future. Global Change Biology. 2003;9(4):479–92. https://doi.org/10.1046/j.1365-2486.2003.00629.x
25. Chu H, Luo X, Ouyang Z, Chan WS, Dengel S, Biraud SC, et al. Representativeness of Eddy-Covariance flux footprints for areas surrounding AmeriFlux sites. Agricultural and Forest Meteorology. 2021;301–302:108350. https://doi.org/10.1016/j.agrformet.2021.108350
26. Lübben A, Leven C. The Starzach site in Southern Germany: a site with naturally occurring CO2 emissions recovering from century-long gas mining as a natural analog for a leaking CCS reservoir. Environ Earth Sci. 2018;77(8). https://doi.org/10.1007/s12665-018-7499-y
27. Büchau YG, van Kesteren B, Platis A, Bange J. An Autarkic Wireless Sensor Network to Monitor Atmospheric CO2 Concentrations. metz. 2022;31(4):331–45. https://doi.org/10.1127/metz/2022/1125
28. Büchau YG, Leven C, Bange J. A portable low-cost device to quantify advective gas fluxes from mofettes into the lower atmosphere: first application to Starzach mofettes (Germany). Environ Monit Assess. 2024;196(2). https://doi.org/10.1007/s10661-023-12114-8
29. Lübben A, Leven C. A gas-flow funnel system to quantify advective gas emission rates from the subsurface. Environ Earth Sci. 2022;81(15). https://doi.org/10.1007/s12665-022-10512-8
30. Herrmann K. Design reiteration of a chimney gas flowmeter for natural CO2 emissions from mofettes: differential pressure measurement increases resolution and accuracy. 2023. https://doi.org/10.15496/PUBLIKATION-89337
31. Rogie JD, Kerrick DM, Chiodini G, Frondini F. Flux measurements of nonvolcanic CO2 emission from some vents in central Italy. J Geophys Res. 2000;105(B4):8435–45. https://doi.org/10.1029/1999jb900430
32. Bell C, Ilonze C, Duggan A, Zimmerle D. Performance of continuous emission monitoring solutions under a single-blind controlled testing protocol. Environ Sci Technol. 2023;57(14):5794–805. https://doi.org/10.1021/acs.est.2c09235
33. Krause K, Wittrock F, Richter A, Busch D, Bergen A, Burrows JP, et al. Determination of NOx emission rates of inland ships from onshore measurements. Atmos Meas Tech. 2023;16(7):1767–87. https://doi.org/10.5194/amt-16-1767-2023
34. Jia M, Fish R, Daniels WS, Sprinkle B, Hammerling D. A fast and lightweight implementation of the Gaussian puff model for near-field atmospheric transport of trace gasses. Sci Rep. 2025;15(1):18710. https://doi.org/10.1038/s41598-025-99491-x PMID: 40437081
35. Osher S, Fedkiw R. Signed distance functions. In: Osher S, Fedkiw R, editors. Level set methods and dynamic implicit surfaces. New York, NY: Springer. 2003. p. 17–22.
36. Simmonds JG. The gradient, the del operator, covariant differentiation, and the divergence theorem. In: Simmonds JG, editor. A brief on tensor analysis. New York, NY: Springer; 1994. p. 71–105.
37. Yamartino R. Gaussian puff modelling. Air quality modeling - theories, methodologies, computational techniques, and available databases and software. The EnviroComp Institute and the Air & Waste Management Association; 2008. p. 281–314.
38. Gifford FA. Tropospheric relative diffusion observations. J Appl Meteor. 1977;16(3):311–3. https://doi.org/10.1175/1520-0450(1977)016<0311:trdo>2.0.co;2
39. Edinger JG. A technique for measuring the detailed structure of atmospheric flow. In: International Symposium on Atmospheric Turbulence in the Boundary Layer. 1952. p. 241.
40. Measurement and analysis of puff dispersion above the atmospheric boundary layer using quantitative imagery. Journal of Applied Meteorology. 2002;41(10):1027–41. https://doi.org/10.1175/1520-0450(2002)041<1027:maaopd>2.0.co;2
41. Cao X, Roy G, Hurley WJ, Andrews WS. Dispersion coefficients for Gaussian Puff models. Boundary-Layer Meteorol. 2011;139(3):487–500. https://doi.org/10.1007/s10546-011-9595-3
42. Hanna SR, Briggs GA, Hosker J. Handbook on Atmospheric Diffusion. Oak Ridge, TN (USA): National Oceanic and Atmospheric Administration; 1982.
43. Griffiths RF. Errors in the use of the Briggs parameterization for atmospheric dispersion coefficients. Atmospheric Environment. 1994;28(17):2861–5. https://doi.org/10.1016/1352-2310(94)90086-8
44. Manheim DC, Newman S, Yeşiller N, Hanson JL, Guha A. Application of cavity ring-down spectroscopy and a novel near surface Gaussian plume estimation approach to inverse model landfill methane emissions. MethodsX. 2023;10:102048. https://doi.org/10.1016/j.mex.2023.102048
45. A theory of eddy diffusion in the atmosphere. Proc R Soc Lond A. 1932;135(826):143–65. https://doi.org/10.1098/rspa.1932.0025
46. Turner DB. Workbook of atmospheric dispersion estimates. Washington, D.C.: U.S. Government Printing Office/United States Environmental Protection Agency, Office of Air Programs; 1973.
47. EPA. Workbook for Plume Visual Impact Screening and Analysis (Revised). EPA-454/R-92-023. United States: Office of Air Quality Planning and Standards. 1992.
48. Walcek C. A Gaussian Dispersion/Plume Model Explicitly Accounting for Wind Shear. 13th Joint Conference on the Applications of Air Pollution Meteorology with the Air and Waste Management Association. 2004;.
49. Büchau Y. CO2 time series data of eleven sensor stations in summer 2022 at the Starzach site in south-western Germany. 2025. https://doi.org/10.5281/zenodo.17055782

50. Virtanen P, Gommers R, Oliphant TE, Haberland M, Reddy T, Cournapeau D, et al. SciPy 1.0: fundamental algorithms for scientific computing in Python. Nat Methods. 2020;17(3):261–72. https://doi.org/10.1038/s41592-019-0686-2

51. Huiru W, Zhanping Y, Fan M, Bin L, Peng H. Study on dispersion of carbon dioxide over the Shrubbery Region. Front Energy Res. 2021;9. https://doi.org/10.3389/fenrg.2021.695224

52. Stull RB. An introduction to boundary layer meteorology. Stull RB, editor. Dordrecht: Springer Netherlands. 1988.

53. Büchau YG, Mashni H, Bramati M, Savvakis V, Schäfer I, Jung S, et al. PARMESAN: meteorological timeseries and turbulence analysis backed by symbolic mathematics. JOSS. 2024;9(94):6127. https://doi.org/10.21105/joss.06127

54. Meurer A, Smith CP, Paprocki M, Čertík O, Kirpichev SB, Rocklin M, et al. SymPy: symbolic computing in Python. PeerJ Computer Science. 2017;3:e103. https://doi.org/10.7717/peerj-cs.103

55. Hunter JD. Matplotlib: a 2D graphics environment. Comput Sci Eng. 2007;9(3):90–5. https://doi.org/10.1109/mcse.2007.55